Improving volume-averaged simulations of matrix-stabilized combustion through direct X-ray μCT characterization: Application to NH_3/H_2-air combustion

Thorsten Zirwes[a,b,c,1], Guillaume Vignat[a,*], Edna R. Toro[a], Emeric Boigné[a], Khaled Younes[a], Dimosthenis Trimis[c], Matthias Ihme[a,d]

[a] Department of Mechanical Engineering, Stanford University, Stanford CA 94305, USA
[b] Steinbuch Centre for Computing, Karlsruhe Institute of Technology, Herrmann-von-Helmholtz-Platz 1, Eggenstein-Leopoldshafen 76344, Germany
[c] Engler-Bunte-Institute, Division of Combustion Technology, Karlsruhe Institute of Technology, Engler-Bunte-Ring 1, Karlsruhe 76131, Germany
[d] Department of Photon Science, SLAC National Accelerator Laboratory, Menlo Park, CA 94025, USA

Keywords:
Matrix stabilized combustion
Volume-averaged modeling
Ammonia combustion
X-ray computed microtomography

A B S T R A C T

Porous media combustion (PMC) relies on internal heat recirculation in an open-cell ceramic foam matrix to enhance the flame speed of fuels with poor combustion properties. Volume-averaged simulations are often used to study the combustion performance and pollutant emissions of such systems. However, due to the varying complexity of matrix geometries found in practical burners, as well as the wide range of closure models for the constitutive relations of the solid phase, contradicting statements about the predictive accuracy of these volume-averaged models can be found in the literature. In this work, we propose an open-source modeling framework for accurate volume-averaged PMC simulations by using first-principles methods to determine effective properties used in closure models. This framework relies on adequately characterizing the topology of the solid matrix, using commonly available X-ray computed microtomography. With this approach, significant improvements in accuracy are reported compared to empirical models from the literature. The framework based on first-principle evaluations of constitutive relations is compared against experimental measurements conducted on an interface-stabilized burner operated with premixed NH_3/H_2-air. The model shows good agreement for exhaust gas composition and stability limits. The proposed simulation framework performs significantly better than state-of-the-art techniques that employ commonly used empirical correlations for effective matrix properties.

Statement of Significance: We present a new open-source simulation framework for improved characterization of porous media combustion. By utilizing μCT techniques, accurate effective matrix properties can be determined from first-principle simulations. These effective properties are used in closure models for 1D volume-averaged reacting flow simulations using appropriate sub-models for heat recirculation. This modeling framework is able to reliably predict stability limits while conventional closure models yield erroneous trends. Assessment of the resulting modeling framework is performed using experiments with exhaust gas characterization performed on a NH_3/H_2-air porous media burner.

1. Introduction

The transition towards low-carbon combustion devices is a promising solution to reduce net greenhouse gas emissions. Low-carbon fuels such as hydrogen (H_2), ammonia (NH_3), and low-heating-value syngas and biogas are therefore subjects of active research. However, most of these fuels exhibit poor combustion properties, making it difficult to stabilize flames in conventional combustion devices [1–3]. One solution is the use of porous media combustion (PMC) [4–6]. These burners consist of an open-cell ceramic matrix. Heat recirculation to the reaction zone by conduction and radiation within the solid matrix can significantly increase the flame speed. This is helpful to stabilize combustion processes when using fuels with poor combustion properties [7–12].

Numerical simulations of PMC can assist with understanding, designing, and optimizing porous media burners (PMBs) [4,6,13]. Different simulation concepts have been developed to model PMC,

* Corresponding author.
E-mail address: gvignat@stanford.edu (G. Vignat).
[1] Currently at the Institute for Combustion Technology, University of Stuttgart, Pfaffenwaldring 31, Stuttgart 70569, Germany.

including pore-resolved simulations and volume-averaged methods. Direct pore-level simulations (DPLS) generally couple a 3D fully resolved finite-volume reacting flow simulation with a 3D thermal simulation of the solid. DPLS can yield accurate results, but they require the full resolution of the flame structure and of radiative and diffusive transport in the complex pore topology [14–16]. This stringent requirement makes their computational cost and complexity high, typically limiting their application beyond fundamental research.

In contrast, volume-averaged methods are a popular concept for low-order simulations of PMC. In particular, 1D volume-averaged simulations (1D–VAS) describe the 1D flame structure in porous media and are frequently employed in practical applications. While the computational cost is low, these simulations require appropriate closure models to describe the solid phase, the inter-phase heat transfer, and other constitutive properties. This requires the accurate determination of effective properties accounting for effects of the solid geometry [15,17]. The present work focuses on 1D–VAS and their ability to capture engineering quantities of interest, such as stability limits and pollutant emissions. In what follows, we will briefly review modeling approaches typically used in 1D–VAS.

Lawson and Norbury [18] performed one of the first 1D–VAS for porous media applications, and since then, conflicting reports about the predictive capabilities of volume-averaged simulations have been published [6]. For example, in [17,19–23], the authors have reported good agreement between 1D–VAS and reference data. By contrast, in [24–30], 1D–VAS were unable to reproduce experimental measurements. These studies cover a large range of burner configurations, from open-cell ceramic foam burners, to filtration combustion and packed bed reactors, with applications ranging from gas-turbine combustors, heat production in process burners, to fuel reforming and hydrogen production. The aforementioned studies highlight that the predictive capability of 1D–VAS for matrix-stabilized combustion heavily depends on the choice of closure models for inter-phase heat transfer, tortuosity, and heat transport by conduction and radiation within the solid matrix. These studies also indicate that 1D–VAS have a strong sensitivity to effective solid matrix properties. Therefore, direct and accurate measurements of these properties tend to yield more predictive 1D–VAS.

Radiative heat transfer is one of the dominant processes of heat recirculation in the solid matrix, and is among the closure models that has received the most attention for PMC modelling [6]. The Rosseland model is a popular approach for modeling radiative transport [18,19,24,29,31,32]. It relies on modeling radiative processes in the solid as an effective heat conduction coefficient. However, this model has been shown to yield considerable discrepancies when compared with experimental measurements [6]. Nonetheless, it is still commonly used today for its simple implementation. The P3 model is another approach, proposed by Barra et al. [25] and Henneke and Ellzey [33], who applied it to low velocity filtration combustion. It approximates the solution of the radiation transport equation using an analytical ansatz function. Another approach is to directly solve the full radiation transport equation (RTE). This approach is accurate, but also significantly more computationally intensive [22,34]. The Schuster-Schwarzschild model [35], successfully used by Sobhani et al. [17,23], is a cost-effective alternative to solving the full RTE for conditions in which the solid can be assumed to be a gray body. It relies on solving a set of coupled ordinary differential equations to compute the two components of the axial radiative flux. The effect of the solid geometry is incorporated using effective radiative properties, which can be computed a-priori using inexpensive ray-tracing simulations.

Solid heat conduction of the matrix is another important process for heat recirculation and flame stabilization. The determination of effective heat conduction properties for volume-averaged simulations requires both a good characterization of the bulk material's property, which is often lacking for high temperature engineered ceramics used in PMBs [36], and a good model to account for the effect of the solid matrix' macroporosity. Concerning the latter, a simplified approach in which the material conductivity is multiplied by the volume fraction of the solid inside the control volume is sometimes used [37–39]. Depending on the geometry of the solid, the actual effective value can differ significantly [36,40]. A better estimate can be obtained by performing additional thermal simulations using the geometry of the solid structure. This can be obtained using a thermal finite volume solver on a geometrical grid obtained from x-ray micro-computed-tomography (µCT) [15,17,36,41].

In addition to heat recirculation within the solid matrix, other physical phenomena have to be considered for 1D–VAS, namely inter-phase heat transfer, gas-phase tortuosity, and flame wrinkling. Heat transfer between the solid and the gas phase is usually modeled with a volumetric heat transfer coefficient, derived from Nusselt number correlations dependent on the flow regime and the solid geometry. These correlations are most often determined from non-reactive flows using either experimental measurements or DPLS [17,19,29,39,42–49]. The porous matrix also affects diffusive processes in the gas phase by increasing characteristic transport length scales, a phenomena known as tortuosity. This can be taken into account by decreasing the diffusion coefficients found in the 1D–VAS governing equations for gas-phase temperature and species [50]. In practice, the effect of tortuosity for combustion applications in PMBs is often neglected [17,22]. While different correlations exist that relate tortuosity to pore size, porosity, or Péclet number [20,25,26,42,46,51], their validity is often limited. Alternatively, effective tortuosity properties can be computed from high resolution tomographic images of the solid matrix [19,29,52]. In recent years, new correlations have also been derived using machine learning approaches [53,54].

Table 1 presents a synthesis of closure models commonly employed in 1D–VAS.

In this work, we present a framework for 1D–VAS. We hypothesize that the reliability of 1D–VAS can be improved by utilizing accurate effective properties for closure models. With modern tools such as ceramic additive manufacturing and µCT [36], the detailed macro-porous structure of the ceramic matrix is often readily accessible and can be utilized to accurately derive these effective properties by performing separate, inexpensive 3D simulations based on first-principles. These effective properties can then be utilized to perform 1D–VAS reacting flow simulations. We refer to this approach as the 1D–VAS–FP framework (1D Volume-Averaged Simulations with closure models derived from First Principles).

In the present work, we introduce an open-source tool-chain that implements the 1D–VAS–FP framework and applies it to a foam geometry characterized using high-resolution µCT. The closure models used in our implementation of the 1D–VAS–FP framework are highlighted in bold font in Table 1. The test case for the evaluation of the 1D–VAS–FP framework is an interface-stabilized PMB, described in Section 2, that was recently studied in [56]. Matrix-stabilized premixed NH_3/H_2-air combustion was studied over a wide range of operating conditions and fuel mixture compositions. The 1D–VAS–FP framework and tool-chain are introduced and described in detail in Section 3. Results are presented in Section 4.1, which assesses the ability of 1D–VAS–FP simulations to accurately capture the stability limit of the burner. To provide a comparative reference, 1D–VAS simulations are also conducted using state-of-the-art empirical closure models and correlations. This is thereafter referred to as the 1D–VAS–EMP framework (1D Volume-Averaged Simulations with EMPirical closure models). In Table 1, closure models used for 1D–VAS–EMP simulations are in-

Table 1
Literature review on closure models used in 1D–VAS for PMBs. The models indicated **in bold** are those used in the 1D–VAS–FP framework described in the present work. Those *in italic* are used in the 1D–VAS–EMP framework employed as a reference in the present work.

Physical process	Modeling approach	Reference
Solver adapted from	Chemkin (closed source)	[19,20,26,29,33,34,51]
	Cantera (closed source)	[15,17,32]
	Cantera (open-source)	**present work**
Chemical mechanism	Reduced	[27]
	Detailed	[15,17,19,20,22,26,51], **present work**
Radiation	*Rosseland model*	[18,19,24,29,31,32]
	P3	[25,26,33]
	Schuster-Schwarzschild	[17,23]
	Schuster-Schwarzschild with properties from μCT	**present work**
	Full Radiative Transfer Equation	[22,34]
Solid heat conduction	*Derived from porosity*	[22,24,26,27,32,37–39,51]
	3D simulations from μCT	[15,17,19,29,40,41,55], **present work**
Inter-phase heat transfer	***Derived from non-reacting experiments/DPLS***	[17,22,24,26,27,29,31,39,42–49], **present work**
	Derived from reacting experiments/DPLS	[15,29]
Gas-phase diffusion	*Neglected*	[17,22]
	Tortuosity from correlation	[20,25,26,42,46,51]
	3D simulation from μCT	[15,19,29], **present work**

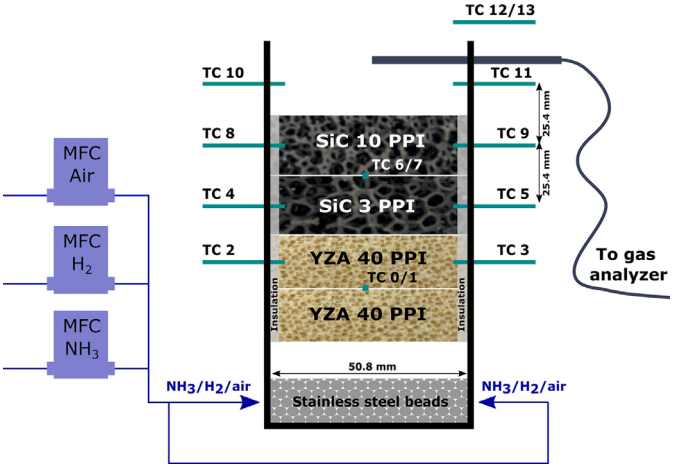

Fig. 1. Schematic of the experimental apparatus (not to scale). MFC: mass flow controller; SiC: silicon carbide; YZA: yttria-stabilized zirconia alumina; TC: thermocouple. Reproduced from Vignat et al. [56].

dicated using italic. 1D–VAS–FP and 1D–VAS–EMP are compared in Section 4.2. The focus is then placed on pollutant emissions: we first assess the accuracy of the 1D–VAS–FP framework by comparing with experiments in Section 4.3. In Section 4.4, we focus on a more fundamental analysis of PMB-stabilized NH_3 combustion using insights from 1D–VAS–FP simulations. Conclusions are presented in Section 5.

2. Experimental setup, instrumentation, and measurements

The experimental measurements used in the present work were published in [56], and we refer the reader to this reference for a more detailed description of the experimental setup. The burner depicted in Fig. 1 is of an interface-stabilized design, with three axially staged sections. It has an outer diameter of 50.8 mm. The perfectly premixed reactants first flow through two blocks of 25.4 mm-long 40 pores per inch (PPI) open-cell yttria-stabilized zirconia alumina (YZA, with 2% calcium oxide, 2% yttria, 62% zirconia, and 34% alumina by weight) foam manufactured by Selee (Hendersonville, NC, USA), acting as flame arrestor. These blocks are followed by two 25.4 mm-long blocks of SiC foams manufactured by Ultramet (Pacoima, CA, USA). The first of these two blocks has a larger pore size (3 PPI) than the second (10 PPI). The burner is designed such that combustion occurs within these SiC ceramic foams [5]. Note that the PPI ratings used to describe these ceramic foams are a commercial designation.

The flow of reactants is controlled by mass flow controllers (Alicat, Tucson, AZ, USA) and all reactants are premixed upstream of the burner's inlet. The uncertainties on the reported equivalence ratios and mass flow rates are 1.6% and 0.8%, respectively. The experiments are conducted at ambient pressure and temperature. Gas analysis is performed in the exhaust of the burner. NO, O_2, NH_3, and H_2 concentrations are reported in dried exhaust gases. NO and NH_3 emissions are normalized to 15% O_2 following standard practice [57]. Experimental uncertainties on these measurements are 20%, 15% and 7%, respectively, for normalized NO, normalized NH_3 and H_2, respectively [56].

3. 1D modeling framework

3.1. Governing equations and constitutive relations

In the present work, we consider a PMB with constant cross-section and an axial flow direction represented with coordinate x. In this model, we invoke the following assumptions:

i. The solid phase is chemically inert with no catalytic effects,
ii. Radiation within the gas phase and between the solid and gas is negligible,
iii. Dufour and Soret effects are negligible,
iv. Viscous dissipation is negligible,
v. The flow has a variable density, but can be treated as incompressible,
vi. The axial pressure gradient within the burner has negligible effects on the chemistry, and on heat and species transport, and
vii. Turbulent effects are negligible given the low Reynolds number of the flow.

The 1D volume-averaged governing equations comprise the balance equations for mass, species, and temperature of the gas phase as [17,22,29,58]

$$\frac{\partial(\rho_g \varepsilon_v)}{\partial t} + \frac{\partial}{\partial x}\left(\varepsilon_v \rho_g u\right) = 0, \tag{1}$$

$$\frac{\partial(\rho_g \varepsilon_v Y_k)}{\partial t} + \frac{\partial}{\partial x}\left(\varepsilon_v \rho_g Y_k u\right) = -\frac{\partial}{\partial x}\left(\varepsilon_v j_k\right) + \varepsilon_v \dot{\omega}_k, \tag{2}$$

$$c_{p,g}\frac{\partial(\rho_g\varepsilon_v T_g)}{\partial t}+c_{p,g}\frac{\partial}{\partial x}\left(\varepsilon_v\rho_g T_g u\right)$$
$$=\frac{\partial}{\partial x}\left(\varepsilon_v\frac{\lambda_g}{\eta}\frac{\partial T_g}{\partial x}\right)-\varepsilon_v\left(\sum_{k=1}^{N_s}c_{p,k}j_k\right)\frac{\partial T_g}{\partial x}$$
$$-h_v(T_g-T_s)+\varepsilon_v\dot{q}_{\text{chem}}, \tag{3}$$

where the subscripts g and s denote the gas and solid phase, respectively, ρ is the density, ε_v is the porosity, u is the interstitial axial velocity, Y_k is the mass fraction of the kth species, j_k is its diffusive mass flux, and $\dot{\omega}_k$ is its reaction rate. T is the temperature, c_p the isobaric heat capacity of the mixture, $c_{p,k}$ the isobaric heat capacity of the kth species, N_s is the number of species, λ the gas-phase heat conductivity, η is the tortuosity factor, h_v is the volumetric inter-phase heat transfer coefficient, and $\dot{q}_{\text{chem}}$ is the heat release rate associated with chemical reactions.

In the gas phase, the diffusive mass flux of each species j_k in Eq. (2) is modeled with the Curtiss-Hirschfelder approximation and includes tortuosity effects [59]:

$$j_k=-\rho_g\frac{M_k}{M}\frac{D_k}{\eta}\frac{\partial X_k}{\partial x}+Y_k\rho_g\sum_{i=1}^{N_s}\frac{M_i}{M}\frac{D_i}{\eta}\frac{\partial X_i}{\partial x}, \tag{4}$$

where M_k and X_k are the molar mass and the mole fraction of the kth species, D_k its diffusion coefficient, and M is the mean molecular weight. Heat transfer between solid and gas phase is modeled by a volumetric heat transfer coefficient h_v, which is computed as [29]

$$h_v=Nu\frac{S_v\lambda_g}{d_h}, \tag{5}$$

where S_v is the specific surface of the porous matrix and $d_h=4\varepsilon_v/S_v$ is the hydraulic diameter of the porous medium. The Nusselt number, Nu, is computed from the correlation by Bedoya et al. [29]

$$Nu=3.7Re^{0.38}Pr^{0.25}, \tag{6}$$

with the Reynolds and Prandtl numbers based on the gas-phase properties

$$Re=\frac{\rho_g u d_h}{\mu_g},\quad Pr=\frac{c_{p,g}\mu_g}{\lambda_g}, \tag{7}$$

where μ_g is the viscosity of the gas phase.

The governing equation for the solid-phase temperature T_s is

$$(1-\varepsilon_v)\rho_s c_s\frac{\partial T_s}{\partial t}=\frac{\partial}{\partial x}\left(\lambda_{\text{eff}}\frac{\partial T_s}{\partial x}\right)-\dot{q}_{\text{rad}}-\dot{q}_{\text{loss}}+h_v(T_g-T_s), \tag{8}$$

where c_s is the heat capacity of the solid, λ_{eff} is the effective heat conductivity, $\dot{q}_{\text{rad}}$ is the radiative heat transfer source term, and $\dot{q}_{\text{loss}}$ is the source term for heat losses through the outer radial boundary of the burner.

Heat recirculation due to radiation is an essential process to describe interface-stabilized PMC. Under a gray body assumption, we model axial heat transport by radiation with the Schuster-Schwarzschild model [17,23,35], where $\dot{q}_{\text{rad}}$ in Eq. (8) is computed from the contribution of radiative flux in positive axial direction $\dot{q}_{\text{R}}^{+}$ and negative axial direction $\dot{q}_{\text{R}}^{-}$,

$$\dot{q}_{\text{rad}}=2\beta(1-\omega_{\text{rad}})(2\sigma T_s^4-[\dot{q}_R^{+}+\dot{q}_R^{-}]), \tag{9}$$

where σ is the Stefan–Boltzmann constant. The extinction coefficient β is directly computed from the µCT scans. The scattering albedo ω_{rad} is computed using a gray body assumption as [60,61]

$$\omega_{\text{rad}}=\frac{1}{2}(2-e_{\text{rad}}), \tag{10}$$

where e_{rad} is the emissivity of the solid surface.

Table 2
Boundary conditions for 1D–VAS.

Quantity	Inlet	Outlet
u	fixed	zero gradient
Y_k	fixed mass flux	zero gradient
T_g	300 K	zero gradient
T_s	300 K	$\lambda_{\text{eff}}\frac{\partial T_s}{\partial x}+e_{\text{rad}}\sigma(1-\varepsilon_v)(T_s^4-T_{\text{amb}}^4)=0^{\dagger}$
$\dot{q}^{+}$	σT_{amb}^4	–
$\dot{q}^{-}$	–	σT_{amb}^4

† The outlet boundary condition for T_s models the radiative heat flux from the top solid surface of the burner to the ambience. Heat losses to the ambience on the outer cylindrical boundary of the burner are modeled using a volumetric source term, Eq. (13).

To determine $\dot{q}_{\text{R}}^{+}$ and $\dot{q}_{\text{R}}^{-}$, two linear ordinary differential equations are solved [35]:

$$\frac{\mathrm{d}\dot{q}^{+}}{\mathrm{d}x}=-\beta(2-\omega_{\text{rad}})\dot{q}^{+}+\beta\omega_{\text{rad}}\dot{q}^{-}+2\beta(1-\omega_{\text{rad}})\sigma T_s^4, \tag{11}$$

$$-\frac{\mathrm{d}\dot{q}^{-}}{\mathrm{d}x}=-\beta(2-\omega_{\text{rad}})\dot{q}^{-}+\beta\omega_{\text{rad}}\dot{q}^{+}+2\beta(1-\omega_{\text{rad}})\sigma T_s^4. \tag{12}$$

In addition to the axial radiative heat transport, radial radiative heat loss through the outer insulation layer is taken into account as

$$\dot{q}_{\text{loss}}=\frac{4\sigma e_{\text{rad}}\tau}{D}(T_s^4-T_{\text{amb}}^4). \tag{13}$$

In this 1D model, heat losses are represented as volumetric sources, assuming a cylindrical burner with an outer diameter D and transmissivity of the insulation layer τ. T_{amb} is the ambient temperature, here assumed to be 300 K. Heat losses due to conduction and convection on the outer cylindrical boundary of the burner are neglected in the present work, as they are estimated to be an order of magnitude smaller than losses due to radiative processes. The derivation of Eq. (13) and the estimation of convective heat losses are detailed in the supplementary materials.

The boundary conditions for the governing equations are summarized in Table 2.

In this work, we use the reaction mechanism proposed by Stagni et al. [62] for NH_3/H_2-air combustion. This mechanism consists of 29 species and 203 reactions, and has been validated over a wide range of equivalence ratios and H_2 dilutions corresponding to the experimental conditions in [56]. A comparison with other reaction mechanisms [63,64] is included in the supplementary materials.

3.2. Software architecture

Solving the governing equations requires both the determination of effective solid matrix properties and a numerical procedure for solving Eqs. (1)–(13). Therefore, we propose the 1D–VAS–FP framework, a combination of first-principles-based methods for the determination of effective properties and conventional 1D flame modeling software. This framework is summarized in Fig. 2 and utilizes open-source software. Section 3.3 describes the determination of effective matrix properties using first-principle methods. Section 3.4 discusses the numerical implementation of the steady-state solver for governing equations, Eqs. (1)–(3) and (8).

3.3. Determination of effective matrix properties

The governing equations introduced in Section 3.1 include a number of submodels that rely on effective macroporous solid properties to account for 3D effects of the porous matrix. These properties are listed in blue at the center of Fig. 2. To determine these properties, the ceramic foams used in the present work

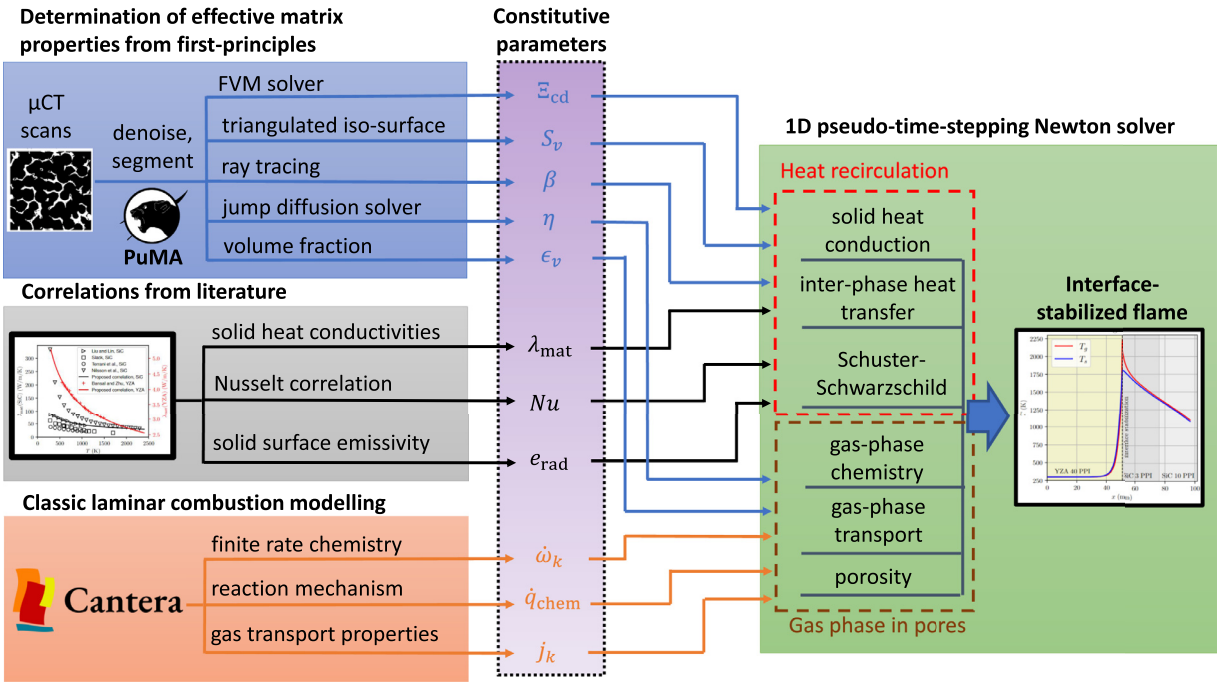

Fig. 2. Summary of the proposed 1D–VAS–FP framework for predictive modeling of 1D volume-averaged simulations for combustion in porous media. All software mentioned above are open-source, including the 1D pseudo-time-stepping Newton solver (green), which is an open-source modification of Cantera [65], available at [66]. (For interpretation of the references to colour in this figure legend, the reader is referred to the web version of this article.)

Table 3
Acquisition parameters for the μCT scans.

Description (units)	YZA	SiC	SiC
Image width (voxel)	2008	2009	2008
Image height (voxel)	2048	2048	2048
Images per scan	2026	2026	2024
Voxel size (μm)	26.4	26.4	25.9
Exposure (s)	3.0	3.0	3.0
x-ray tube voltage (kV)	140.0	60.0	60.0
x-ray tube intensity (mA)	71.0	83.0	83.0

Table 4
Coefficients for the heat conductivity correlations in Eq. (15).

Coefficient (units)	YZA	SiC
λ_s^{ref} (W m^{-1} K^{-1})	91.5	5.33
a	−0.35	−0.53

were characterized using 3D tomographic images obtained with μCT performed on a Zeiss Xradia Versa 520 x-ray microscope (Carl Zeiss Microscopy GmbH, Jena, Germany). The acquisition parameters for the scans are reported in Table 3. After acquisition, the images were denoised using a high-frequency despeckling filter and a non-linear edge preserving filter [67]. Segmentation of the solid and gaseous phases was performed using the method proposed by Otsu [68]. As a final pre-processing step, morphological closing was performed on the images. The resulting 3D models for the three porous foam segments are shown in Fig. 3. In addition to different pore sizes, the morphology of the ceramic lattice shows substantial differences between the YZA and SiC foams. Specifically, the SiC foams manufactured by Ultramet form a lattice of hollow struts, while the YZA foam from Selee has a larger solid structure, which, although pore sizes are similar, has a larger specific surface area.

The effective heat conductivity of the foams was calculated from the temperature-dependent bulk heat conductivity λ_{mat} of the material and an effective thermal conductivity factor Ξ_{cd}, which accounts for macroporosity effects and depends on the topology of the solid matrix

$$\lambda_{eff} = \lambda_{mat}(T_s)\,\Xi_{cd}. \tag{14}$$

Ξ_{cd} is determined from the μCT scans using a finite volume heat transfer solver [69]. The thermal conductivity λ_{mat} of SiC strongly depends on its manufacturing process, with appreciable differences between mono-crystalline SiC obtained by chemical vapor deposition [70,71] and poly-cristalline SiC manufactured using hot pressing and sintering [72–74]. Experimental measurements of λ_{mat} are unfortunately not available for SiC manufactured by the vitreous carbon infiltration process used by our supplier. Measurements from [70–74] are reproduced in Fig. 4. In the present work, we use a correlation based on the data by Liu and Lin [72], whose samples had a similar microporosity to ours, and agrees well with the high-temperature results of Nilsson et al. [70]:

$$\lambda_{mat}(T_s) = \lambda_s^{ref}\left(\frac{T_s}{T_0}\right)^a \tag{15}$$

where $T_0 = 293K$ and the coefficients λ_s^{ref} and a are reported in Table 4. The thermal conductivity of YZA reported in the literature also presents strong variability. This is due to the large design range for the composition of these ceramic materials [75], as well as the strong dependency of YZA's heat conductivity on grain size and microporosity [36,76,77]. The correlations in Eq. (15) were derived from experimental measurements by Bansal and Zhu [75], which best matched the composition of the YZA used in our burner. Their measurements are also reproduced in Fig. 4.

With the exception of the thermal conductivity efficiency factor Ξ_{cd}, all properties computed from μCT require that the hollow struts of the SiC foams are filled. This is accomplished by isolating and filling void volumes that are not connected to the main flow channel using a connectivity tree search algorithm [41]. The porosity ε_v is then computed as the volume fraction of the void voxels.

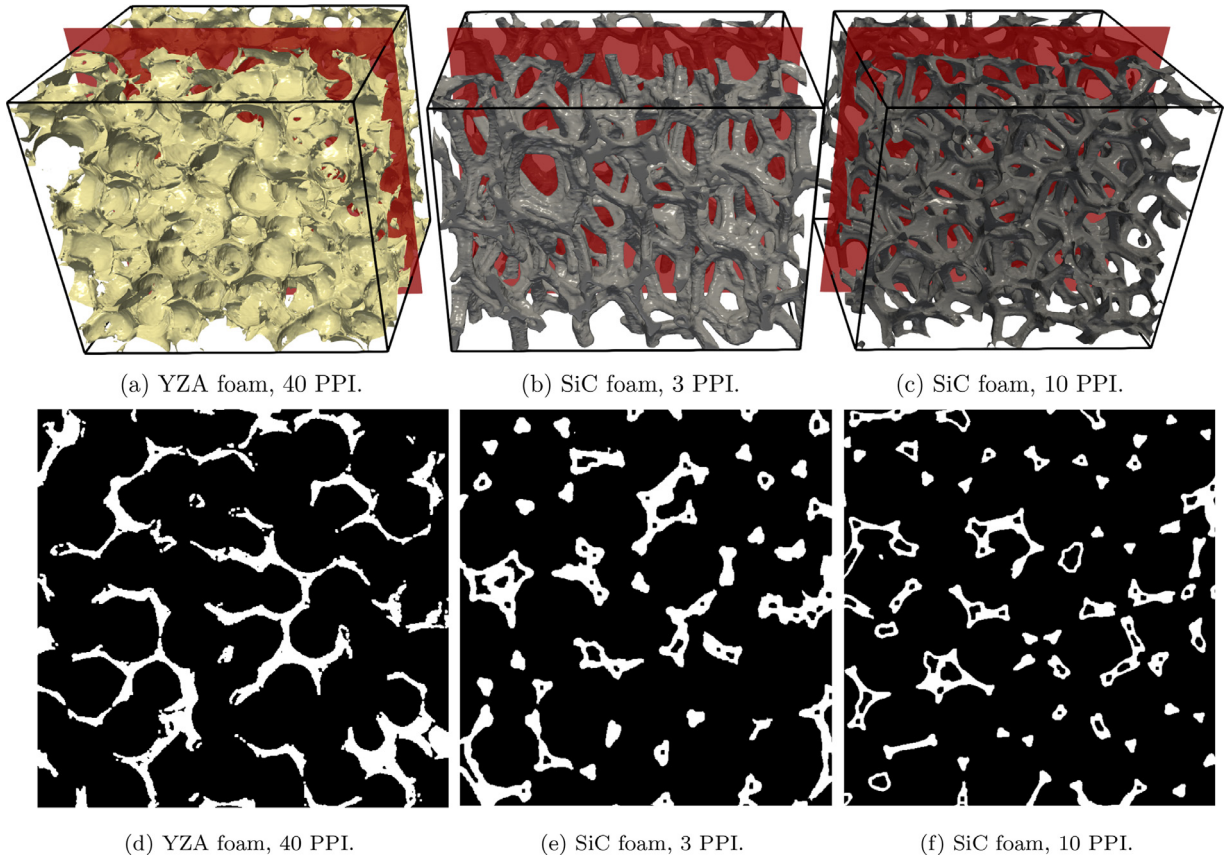

(a) YZA foam, 40 PPI. (b) SiC foam, 3 PPI. (c) SiC foam, 10 PPI.

(d) YZA foam, 40 PPI. (e) SiC foam, 3 PPI. (f) SiC foam, 10 PPI.

Fig. 3. 3D renderings of the CT scans performed for the three different ceramic foams (a)–(c) used in the burner. Red planes show representative cutting planes, given in (d)–(f). White areas are the solid struts, black areas the open pore volume. (For interpretation of the references to colour in this figure legend, the reader is referred to the web version of this article.)

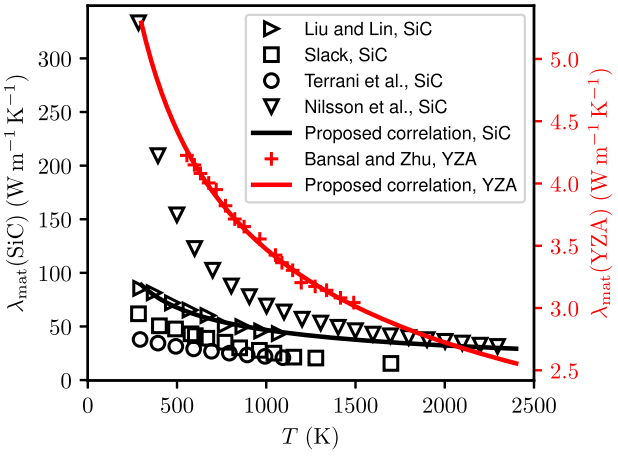

Fig. 4. Experimental measurements of the heat conductivity of YZA and SiC and comparison with the correlation used in the present work, Eq. (15). Bansal and Zhu [75] characterized the heat conductivity of YZA, Liu and Lin [72] that of hot pressed sintered SiC, Slack and Nilsson et al. [70,71] that of single crystal SiC, and Terrani et al. [73] that of 3D printed SiC. The black and red curves show the correlations used in the present work, Eq. (15), with paremeters specified in Table 4. (For interpretation of the references to colour in this figure legend, the reader is referred to the web version of this article.)

To compute the characteristic pore diameter (also known as window diameter) and cell diameter, we use a 3D distance transform watershed algorithm followed by a particle analyzer, both implemented in the PoreSpy toolbox [78,79]. The specific surface area S_v is computed using a triangulated isosurface approximation of the foam structure [41]. The effective solid density is calculated as $\rho_s = m_s/(\pi l r^2(1-\varepsilon_v))$, where m_s is the mass of a foam block, measured on a ZSP-500 scale (Scientech, Boulder, CO, USA), l is its thickness, and r is its radius.

The tortuosity factor η (Eqs. (3) and (4)) models the effect of the increased characteristic length scales of gas-phase diffusion caused by the foam geometry. η is obtained from the µCT using the dedicated explicit jump solver of PuMA [52]. The values of η for the three burner segments are reported in Table 5.

The extinction coefficient β, which is usually determined from empirical models based on the pore diameter and porosity of the solid, is in this work directly calculated for each burner section from ray tracing simulations using the geometry determined from µCT. A large number of point sources are randomly distributed in the void section of the foam. From these points, rays are cast in random directions. The path length of each ray from the light source to the nearest solid is recorded. With a sufficient number of rays and point sources, the inverse mean distance of ray pathways converges to the extinction coefficient [69].

3.4. Numerical implementation and solution strategy

The governing equations and constitutive relations, Eqs. (1)–(13), were implemented in Cantera [65] as an extension to its steady-state 1D reacting flow solver module. Since the numerical methods used in Cantera are well documented [65,80], we focus here on the algorithmic extension to include PMC.

Table 5
Geometric characteristics and effective properties of the porous foams employed in the present work for simulations within the 1D–VAS–FP framework. †: values obtained using μCT and in-house measurements; ⋆: values obtained from the literature.

Description (unit)	YZA	SiC	SiC
Commercial designation (PPI)	40	3	10
Thickness l (mm)	50.8	25.4	25.4
Porosity ε_v (%)	82.5†	86.2†	86.0†
Pore diameter d_p (mm)	1.11†	1.56†	1.07†
Cell size d_c (mm)	2†	3.2†	2.6†
Specific surface S_v (m^{-1})	1,592†	934†	986†
Effective density ρ_s (g cm^{-3})	5.2†	3.21†	3.21†
Material heat conductivity λ_{mat} (W m^{-1} K^{-1})	Eq. (15)⋆	Eq. (15)⋆	Eq. (15)⋆
Axial thermal conductivity efficiency factor Ξ_{cd} (%)	7.2†	5.1†	4.3†
Tortuosity factor η (mm^{-1})	1.34†	1.17†	1.15†
Material emissivity e_{rad}	0.9⋆	0.9⋆	0.9⋆
Extinction coefficient β (m^{-1})	1,340†	526†	683†
Insulation transmissivity τ	0.6	0.6	0.6

First, the gas-phase equations for the balance of total mass, species mass fractions, and gas-phase temperature, Eqs. (1)–(3), are extended by adding the porosity ε_v and tortuosity factor η, which are both a function of the axial coordinate x. All material and effective properties can be assigned arbitrarily as a function of x in our implementation, which is well suited to model the three section burner described in Section 2 and examined in Section 4. Note that the gas-phase governing equations, Eqs. (1)–(3), are formulated to properly account for spatially variable effective properties of the solid porous matrix. The inter-phase heat transfer term is also added to the gas-phase temperature equation solved by Cantera.

Next, an equation for the temperature of the solid-phase is added and coupled to the gas phase solver. The main numerical challenge is the large characteristic time scale associated with the solid-phase temperature equation compared to the gas-phase equations [33]. In addition, our implementation is capable of modelling burners with highly inhomogeneous solid properties typically found in interface stabilized burners [5] and in burner designs leveraging topology gradation [17]. For these reasons and to increase solver robustness, we use a dedicated solution strategy implemented in our modified Cantera solver. A program flow-chart is given in the supplementary materials, Fig. S1. After setting the initial conditions, we solve for the solid-phase temperature T_s in the steady-state formulation while keeping the gas-phase velocity u, temperature T_g, and species mass fractions Y_k constant. For this step, Eigen's [81] direct sparse solver based on supernodal LU factorization and column approximate minimum degree ordering is employed. Next, the residual matrix for the gas-phase governing equations is assembled. For this, the finite difference approach of Cantera is used. A Newton iteration attempts to find a steady-state solution on the current numerical grid. If the Newton step does not converge, a series of pseudo-time steps is performed to find a better initial condition for the next Newton iteration. During both the Newton and pseudo-time steps, the solid-phase temperature is fixed to decouple the gas and solid time scales. Once a steady-state solution for the gas-phase properties is found, the convergence between the solid-phase and gas-phase is checked. If the solid and gas-phase are not converged, this coupled solution procedure is repeated. If both are converged, adaptive mesh refinement is performed if necessary using Cantera's mesh refinement tools. These steps are repeated until the grid refinement criteria are satisfied and both the gas-phase and solid-phase are converged. The computation of the radiation source term $\dot{q}_{rad}$ from Eq. (9) is done using Eigen's direct sparse linear solvers. The supplementary materials give additional information regarding the selection of appropriate initial conditions.

4. Results

4.1. Stability limits

The stability limits of the PMB were experimentally characterized for three different fuel compositions (X_{NH_3} ={100%, 85%, 70%}, with H_2 as balance), as a function of equivalence ratio ϕ and mass flux rate $\dot{m}''$ [56]. Here, stability denotes the stable operation of the burner, where the flame is stabilized at the YZA-SiC interface, and remains as such. In the experiment, this is assessed using thermocouples, whose temperature cannot vary by more than 10 K over 2-min for the condition to be classified as stable. In the simulation, this is assessed by the convergence to a steady-state solution in which the flame is stabilized at the YZA-SiC interface (zero-gradient of temperature at the inlet, peak heat release rates between 25 mm $< x <$ 75 mm). Unstable states refer to conditions of either blowoff of the flame (extinction solution in the simulation, max(T) < 350 K) or flashback of the flame into the YZA foam (inlet-stabilized solution in the simulation, identified by non-zero temperature gradients at the inlet and peak heat release rates located at $x <$ 25 mm).

Predicting the correct stability behavior requires an accurate description of the flame behavior, of the inter-phase heat exchange processes, and—most importantly—of heat recirculation. In PMBs, the latter is one of the main processes determining the location at which the flame stabilizes. Accurate predictions require the modeling of radiative heat transfer and heat conduction through the solid matrix. In the following, we present results obtained using the 1D–VAS–FP framework described in Section 3. Then, in Section 4.2, we will compare the results of the 1D–VAS–FP and 1D–VAS–EMP modelling framework, thereby assessing the importance of accurate determination of effective properties used in closure models.

Figure 5 (a–c) compare the stability maps from experiments and from the 1D–VAS–FP simulations. For X_{NH_3} = 100 % (Fig. 5(a)), the predicted stability map agrees well with the measurements. All measured conditions for stable operation (blue squares) lie within the stable range predicted by the model (blue area). For X_{NH_3} = 85 % (Fig. 5(b)), good agreement for most conditions is found as well. The stable operation range in the experiments extends to slightly higher mass flux rates for near-stoichiometric conditions. At these high flow rates, it is likely that multidimensional effects such as flame front wrinkling, stretch, and local extinctions are present, leading to a thickening of the flame front and a decrease in combustion efficiency [29,82,83]. The 1D volume-averaged model is unable to capture such effects, which might explain the deviation between the simulation and experiments. Furthermore, the model predicts a small flashback region around

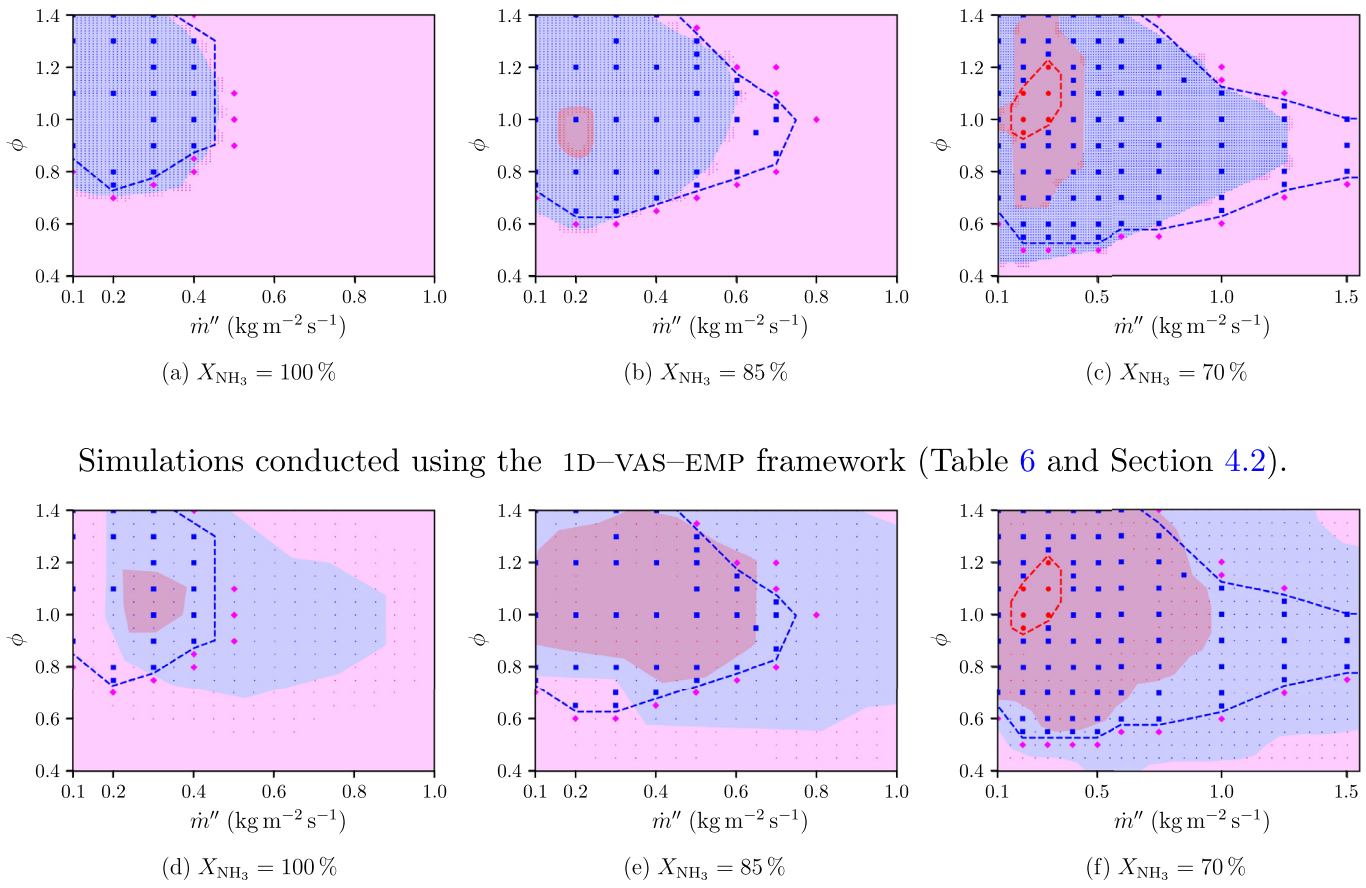

Fig. 5. Stability maps as a function of mass flux rate, $\dot{m}''$, and equivalence ratio, ϕ, from experiments and simulations. Stable burning conditions are represented by the blue regions (simulations) and blue squares (experiments), blowoff by magenta areas (simulations) and magenta diamonds (experiments), and flashback by red areas (simulations) and red circles (experiments). Blue dashed curves mark the stability limits from the experiments. The small dots mark the conditions for which simulations were conducted. (a,d) $X_{NH_3} = 100\%$; (b,e) $X_{NH_3} = 85\%$; and (c,f) $X_{NH_3} = 70\%$. Top row: 1D–VAS–FP framework; bottom row: 1D–VAS–EMP framework. (For interpretation of the references to colour in this figure legend, the reader is referred to the web version of this article.)

$\phi = 0.9$ and $\dot{m}'' = 0.2$ kg.m^{-2}.s^{-1}. Such flashback behavior has been observed experimentally for higher H_2 contents [8,56] and the reason for the existence of these flashback regions within otherwise stable operating conditions is discussed in [56].

Lastly, for $X_{NH_3} = 70$ % (Fig. 5(c)), the differences between measurements and model predictions are more pronounced. Following the trend of the $X_{NH_3} = 85$ % case, the stable operation range extends to higher mass flux rates in the experiments compared to the simulations. Furthermore, the predicted stability range from the simulations extends to slightly leaner conditions at low mass flux rates. The largest difference between measurements and simulations is the over-prediction of the flashback conditions. While a flashback region is present in both the experiments (red dashed curves) and the simulations (red area), it is much more pronounced in simulations, extending up to $\phi = 1.4$ and also to slightly higher mass flux rates.

To quantify the agreement of the stability maps between simulations and experiments more rigorously, we employ the Jaccard index J, given as [84]

$$J = \frac{A_{Exp} \cap A_{Sim}}{A_{Exp} \cup A_{Sim}}, \tag{16}$$

which is formally defined as the area of the intersection of the experimental and simulation data (area of correctly identified stable or unstable region), divided by the union of the areas spanned by all experimental and simulation data (all states). Here, we consider the discrete Jaccard index, which is the sum of all correctly predicted data points divided by all data points. For the cases with $X_{NH_3} = 100$ % (Fig. 5(a)), the model is able to predict 89.6% of experimentally characterized conditions correctly. For $X_{NH_3} = 85$ % cases (Fig. 5(b)), the simulations are able to correctly classify 74.0% of the stability map. For the $X_{NH_3} = 70$ % case (Fig. 5(c)), the Jaccard index is 64.1%, which is mainly due to the overprediction of the flashback region. Nonetheless, the lean blowoff limit is still quantitatively well predicted, even for case $X_{NH_3} = 70$ %.

Figure 6 provides further quantification of the model accuracy in terms of confusion matrices. The confusion matrix is used to assess model prediction quality by comparing ground truth values (here experimental data points) with predicted values (here simulation results) and are for example commonly used in machine learning applications [54]. For each experimental measurement point in Fig. 5, the total number of correctly predicted stable operating conditions (true positives, TP), the number of correctly predicted unstable conditions (true negatives, TN), and wrongly predicted stable conditions (false positives, FP) and wrongly predicted unstable conditions (false negatives, FN) are graphically shown in Fig. 6. The Jaccard index is repeated below each corresponding confusion matrix.

4.2. Direct measurements vs. empirical correlations for constitutive relations and effective properties

As shown in Section 3.3 and Table 5, all effective properties of the porous matrix have been determined in this work from first

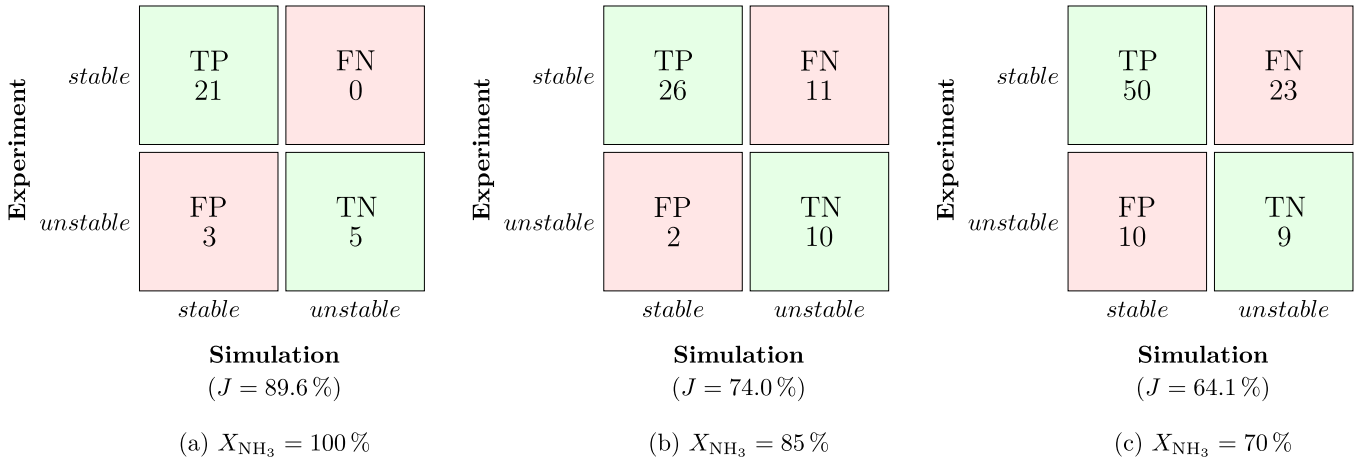

(a) $X_{NH_3} = 100\,\%$ (b) $X_{NH_3} = 85\,\%$ (c) $X_{NH_3} = 70\,\%$

Fig. 6. Confusion matrices for the predicted stability maps, for the three cases reported in Fig. 5(a–c).

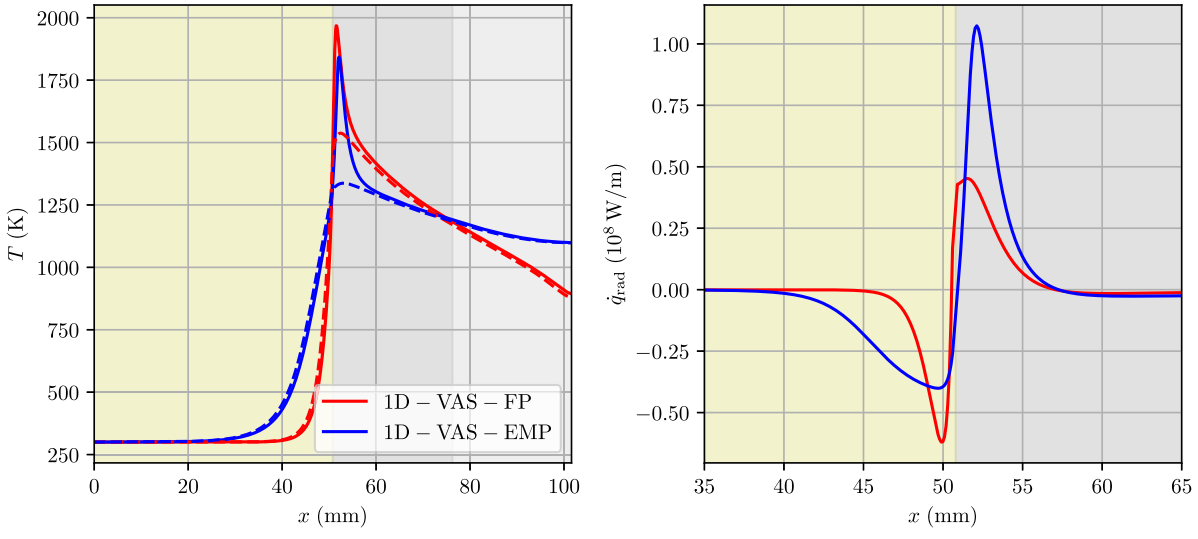

(a) (b)

Fig. 7. Profiles of (a) gaseous temperature (solid curves) and solid temperature (dashed curves) and (b) axial radiative heat source term for $X_{NH_3} = 100\%$, $\phi = 0.9$, and $\dot{m}'' = 0.2$ kg.m^{-2}.s^{-1}. Red curves are results from simulations conducted within the 1D–VAS–FP framework and blue curves from simulations conducted within the 1D–VAS–EMP framework. Yellow shaded region shows the YZA section of the burner, gray shaded section the 3 PPI and 10 PPI SiC sections. (For interpretation of the references to colour in this figure legend, the reader is referred to the web version of this article.)

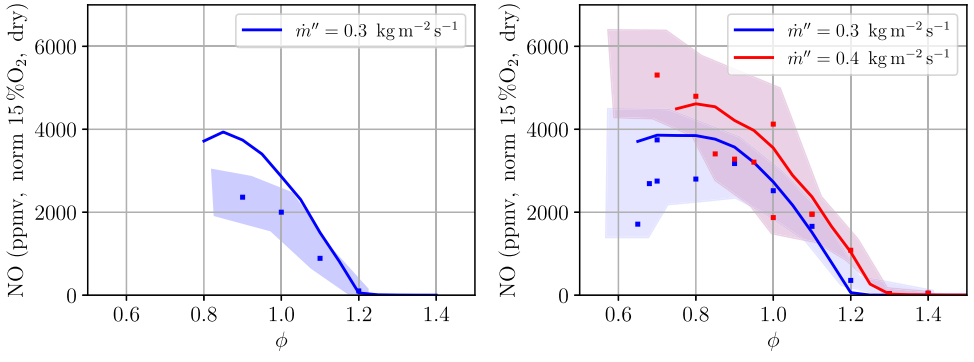

(a) $X_{NH_3} = 100\,\%$ (b) $X_{NH_3} = 85\,\%$

Fig. 8. Measured and simulated NO emissions as a function of equivalence ratio, ϕ, for different values of mass flux rates, $\dot{m}''$. Solid lines show the simulation results, symbols the experimental measurements, and the shaded regions show the experimental uncertainties.

Table 6
Comparison of effective properties used for the extinction coefficient β and thermal conductivity efficiency factor Ξ_{cd} in the 1D–VAS–FP and 1D–VAS–EMP frameworks.

Quantity	1D–VAS–FP framework			1D–VAS–EMP framework		
	YZA 40 PPI	SiC 3 PPI	SiC 10 PPI	YZA 40 PPI	SiC 3 PPI	SiC 10 PPI
	measured			$\beta = 3\frac{\text{PPI}}{0.0254}(1-\varepsilon_v)$ [31]		
β (m^{-1})	1340	526	683	827	49	165
	measured			$\Xi_{cd} = 1-\varepsilon_v$		
Ξ_{cd} (%)	7.2	5.1	4.3	17.5	13.9	14.0

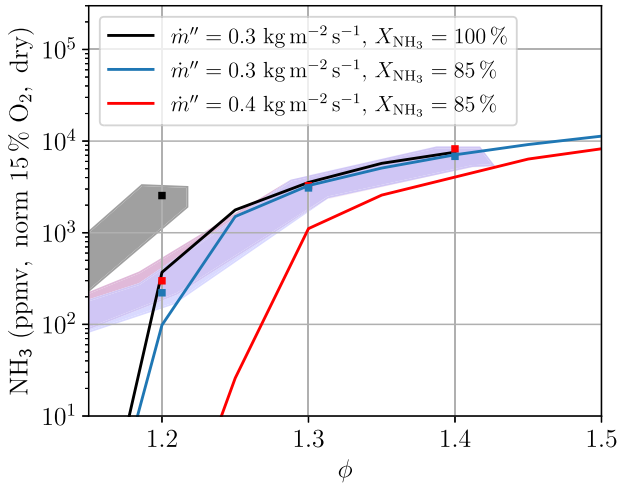

Fig. 9. Measured and simulated unburnt NH_3 emissions as a function of equivalence ratio and different values of mass flux rates. Solid curves show the simulations, symbols the experimental measurements, and the shaded regions show the experimental uncertainties.

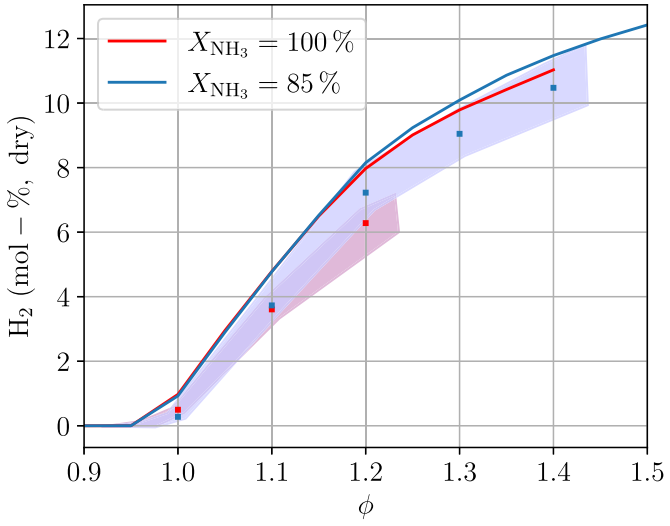

Fig. 10. Measured and simulated unburnt H_2 emissions as a function of equivalence ratio and X_{NH_3} at $\dot{m}'' = 0.3$ kgm^{-2}s^{-1}. Solid lines show the simulation results, symbols the experimental measurements, and shaded regions the experimental uncertainties.

principles, that is from direct 3D measurements of the porous materials used in the burner, as part of the 1D–VAS–FP framework. The material bulk heat conductivities are however based on literature data. To demonstrate the utility of this approach, the simulations have been repeated using the 1D–VAS–EMP framework, that is to say by replacing constitutive relations and effective properties with values derived from commonly employed empirical correlations. Table 1 summarizes the differences in closure models between the frameworks. Table 6 summarizes these changes for two

Table 7
Jaccard index J corresponding to the stability maps of Fig. 5(a–c) and (d–f).

X_{NH_3}	1D–VAS–FP (Fig. 5(a–c))	1D–VAS–EMP (Fig. 5(d–f))
100%	89.6%	44.8%
85%	74.0%	32.7%
70%	64.1%	29.0%

crucial effective properties, the radiative extinction coefficient β and the thermal conductivity efficiency factor Ξ_{cd}. The main differences between the 1D–VAS–EMP and 1D–VAS–FP framework are:

i. The extinction coefficient β is computed from an empirical correlation by Bidi et al. [31];
ii. The efficiency factor for the thermal conductivity of the solid is computed as $\Xi_{cd} = 1 - \varepsilon_v$;
iii. Instead of the Schuster-Schwarzschild model, the simpler Rosseland radiation model is used, where the radiative heat flux is computed as $\dot{q}_{rad} = -16\sigma T_s^3/(3\beta)\nabla T_s$ [35];
iv. Tortuosity effects are neglected ($\eta = 1$).

Using a common empirical correlation, the extinction coefficient β is up to ten times smaller than the value estimated using first-principle measurements. In addition, the heat conductivity in the solid is up to three times higher. To provide a fair comparison, all input parameters for the empirical models, i.e., bulk material heat conductivities and porosities, are set to the same values as those used in the 1D–VAS–FP framework.

Figure 5 (d–f) shows stability maps obtained with the 1D–VAS–EMP framework. In all cases, lean blowoff limits are significantly over-predicted, while the upper blowoff limit extends to far higher mass flux rates than observed in the experiments. Similarly, the flashback regions are largely over-predicted as well, appearing for $X_{NH_3} = 85\%$ (Fig. 5(e)) and even $X_{NH_3} = 100\%$ (Fig. 5(d)). Using the Jaccard index (Eq. (16)), a quantitative comparison between the modeling approaches is reported in Table 7.

Figure 7 compares two flames computed using the 1D–VAS–FP (red) and 1D–VAS–EMP (blue) framework. The operating conditions for both simulations are $X_{NH_3} = 100\%$, $\phi = 0.9$, and $\dot{m}'' = 0.2$ kg.m^{-2}.s^{-1}. Due to the higher heat conductivity of the solid in the 1D–VAS–EMP simulations (larger thermal conductivity efficiency factor, Ξ_{cd}, and lower extinction coefficient, β), the flame is pre-heated more effectively, leading to a broader pre-heat zone that extends far into the YZA section. This effect explains the extended blowoff limits and higher propensity to flashback obtained with 1D–VAS–EMP. Figure 7(b) shows the axial radiative heat transport from the Schuster-Schwarzschild model with measured extinction coefficient (1D–VAS–FP, red curve) and from the Rosseland model with extinction coefficient estimated from a correlation (1D–VAS–EMP, blue curve). The Rosseland model predicts higher heat losses in the exhaust gases, leading to lower peak temperatures for the gas and solid phase at the location of the flame.

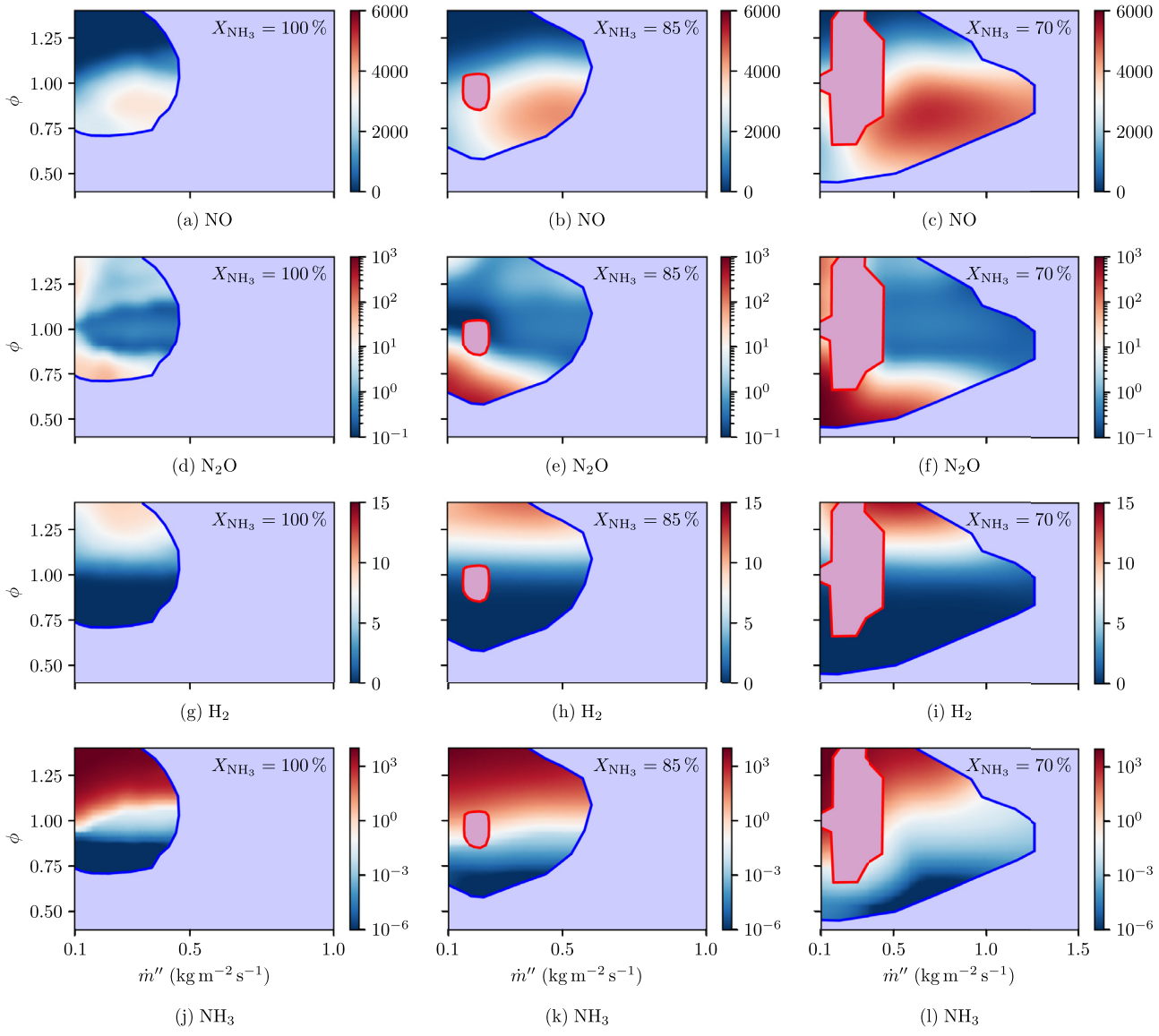

Fig. 11. Emissions of NO (a–c), N_2O (d–f), unburnt H_2 (g–i), and unburnt NH_3 (j–l) as a function of equivalence ratio and mass flux rate for different X_{NH_3}. All emissions, except unburnt H_2, are reported in ppmv, normalized to 15% O_2, dry. H_2 emissions are given in mol-%, dry. The blue curve marks the blowoff limit and the red shaded area the flashback region. (For interpretation of the references to colour in this figure legend, the reader is referred to the web version of this article.)

4.3. Pollutant emissions

Figure 8 compares the NO emissions from the measurements and corresponding simulations for $X_{NH_3} = 100$ % (Fig. 8(a)) and $X_{NH_3} = 85$ % (Fig. 8(b)) as a function of equivalence ratio for different mass flux rates. Due to the overprediction of flashback at $X_{NH_3} = 70$ %, no exhaust gas measurements can be compared with the simulations. The NO formation rate is generally sensitive to the peak temperature in the super-adiabatic region of the flame [1,2]. Thus, the accurate modeling of both heat conduction and radiative heat transfer in the solid is required to obtain a correct estimate for NO emission levels. For $X_{NH_3} = 85$ % (Fig. 8(b)), the predicted NO levels (red and blue curves) lie mostly within the experimental uncertainties (blue and red shaded regions). For the $X_{NH_3} = 100$ % case (Fig. 8(a)), the simulations overpredict NO emissions at lean conditions, where experiments have the largest uncertainties, but still capture the correct trend.

Figure 9 compares measurements of unburnt NH_3 in the exhaust gas with the simulation results. The lower detection limit for experimental measurements lies at about 10 ppmv. Again, for $X_{NH_3} = 85$ % at $\dot{m}'' = 0.3$ kgm^{-2}s^{-1}, all predicted unburnt NH_3 emission levels that are above the detection limits of the experiment fall within 25% of the experimental uncertainties. For $\dot{m}'' = 0.4$ kgm^{-2}s^{-1}, emission levels are underpredicted by 25% for data points above the detection limit of the experiment. Finally, for $X_{NH_3} = 100$ %, only one experimental data point above the detection limit of unburnt NH_3 is available, which is underpredicted by the simulation as well.

Unburnt H_2 was also measured experimentally. It arises from either unburnt H_2 fuel or from NH_3 pyrolysis. The results are reported in Fig. 10. Experimental measurements were only performed for $\dot{m}'' = 0.3$ kgm^{-2}s^{-1}. Again, the predicted H_2 emission levels for the $X_{NH_3} = 85$ % case lie close to the upper limit of the experimental uncertainties (shaded regions). Consistent with the unburnt NH_3 predictions, H_2 emission levels for the $X_{NH_3} = 100$ % case are under-predicted by about 25%.

In summary, the predicted emission levels are within 25% of the measurements for most conditions reported here. Larger discrepancies are found for unburnt NH_3 emissions at certain conditions. This shows that the underlying physical phenomena of heat

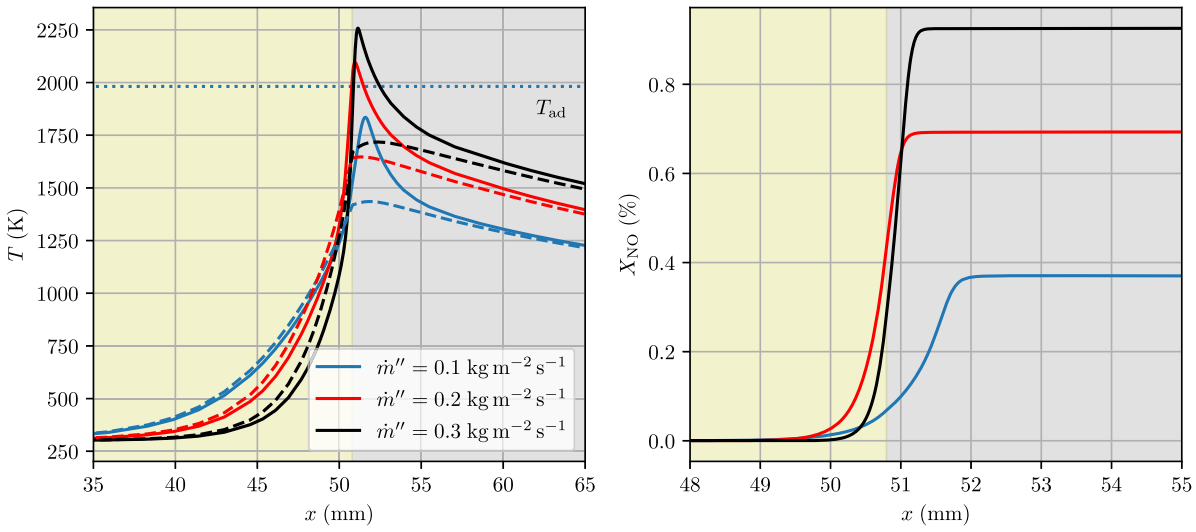

(a) Temperature

(b) NO mole fraction

Fig. 12. Profiles of (a) gaseous temperature (solid curves) and solid temperature (dashed curves) and (b) NO mole fraction for $X_{NH_3} = 100\%$ and $\phi = 0.9$ at different mass flux rates $\dot{m}''$. Yellow shaded region shows the YZA section of the burner and gray shaded region shows the 3 PPI SiC section. The dotted horizontal line marks the adiabatic flame temperature.

recirculation stabilizing the flame at the YZA-SiC interface within the PMB are correctly captured by the model. Trends are also well predicted in all cases.

4.4. Effects of operating conditions on pollutant emissions

This section investigates the influence of operating conditions on pollutant formation and flame structure. In what follows, all simulations were conducted within the 1D–VAS–FP framework. Figure 11 shows the emissions of NO (Fig. 11(a–c)), N_2O (Fig. 11(d–f)), unburnt H_2 (Fig. 11(g–i)), and unburnt NH_3 (Fig. 11(j–l)) as a function of mass flux rate and equivalence ratio for different X_{NH_3} fuel composition. NO emissions present a maximum around $0.8 < \phi < 1.0$, and decrease rapidly under rich conditions. NO emissions also decrease at very lean conditions, around $\phi \approx 0.5$, when flames can be stabilized at such lean conditions. The dependency of NO emissions on mass flux rate is non-monotonic: NO emissions most often increase rapidly with mass flux, up to a maximum ($\dot{m}'' \approx 0.7$ kgm^{-2}s^{-1}), after which it slowly decreases until blowoff occurs. As hydrogen enrichment of the fuel allows the burner to be operated with higher mass flux rates, the globally highest NO emissions appear for $X_{NH_3} = 70\%$. N_2O emissions generally decrease with increasing $\dot{m}''$. The highest N_2O emissions occur in the very lean region. This is similar to what is observed for swirl-stabilized burners [85]. For unburnt H_2 (Fig. 11(g–i)) and NH_3 (Fig. 11(j–l)), the highest concentrations in the exhaust gas occur at rich operating conditions. There is a marked decrease in unburnt NH_3 with increasing $\dot{m}''$, indicating higher NH_3 cracking efficiency within the burner. These observations are in good agreement with experimental results [8,56].

The reason for the change of pollutant emissions with mass flux rate is studied in Fig. 12 for $\phi = 0.9$ and mass flux rates $\dot{m}'' \in \{0.1, 0.2, 0.3\}$ kg.m^{-2}.s^{-1}. Figure 12(a) shows the temperature profiles of three flames at $\phi = 0.9$ and $X_{NH_3} = 100\%$ for different mass flux rates. The flame is in all cases stabilized at the interface between the YZA section of the burner (yellow shaded region) and the 3 PPI SiC section (gray shaded region). As the mass flux rate increases, the volumetric heat release rate correspondingly increases, leading to higher temperatures. Therefore, both the peak gas-phase temperatures (solid curves) and the peak solid-phase temperatures (dashed curves) increase with $\dot{m}''$. For the low mass flux case, the flame is considerably broadened and peak temperatures are below the adiabatic flame temperature (horizontal dotted line) due to heat losses in the burner. Consequently, NO emissions increase with increasing mass flux rate (Fig. 12(b)), due to the strong temperature dependence of NO formation pathways [1]. A more detailed analysis is given in the supplementary materials.

Maximum N_2O emissions are found at lean conditions at sub-adiabatic temperatures, where N_2O is formed preferentially due to lower competition from NO formation. Similarly, the highest unburnt NH_3 emissions are found at rich conditions and at the coldest temperatures, which kinetically limits the decomposition process of NH_3. Inversely, the highest H_2 levels are found at rich operating conditions and high flow rates, where the highest super-adiabatic temperatures are reached and where thermal cracking of NH_3 into H_2 is most intense.

The dependence of the peak temperature on operating conditions is depicted in Fig. 13(a–c) in terms of the difference between the peak gas-phase temperature inside the burner and the corresponding adiabatic flame temperature. With increasing mass flux rates, peak temperatures increase and the burner operates in the super-adiabatic regime. For low mass flux rates, peak temperatures stay below the adiabatic flame temperature. Peak temperatures also tend to decrease near the stoichiometric upper blowoff limit.

Figure 13 (d–f) compares the mass flux rate of the burner, where stable operation can be achieved, with the corresponding mass flux rate of an adiabatic, freely propagating laminar flame, as a function of ϕ. For pure NH_3 flames, mass flux rates can be increased by a factor of six due to the internal heat recirculation and stabilization of the burner. For $X_{NH_3} = 70$ %, a tenfold increase is achieved. This increase towards stable operation at high mass flux rates, and the correspondingly high volumetric power densities, highlights the ability of PMBs to compensate for the generally low flame speeds of NH_3 in practical applications.

5. Conclusions

The present work focuses on 1D volume-averaged simulations of matrix stabilized combustion, with application to the combustion of premixed NH_3/H_2-air blends in an interface-stabilized PMB. We propose a cohesive open-source simulation framework, re-

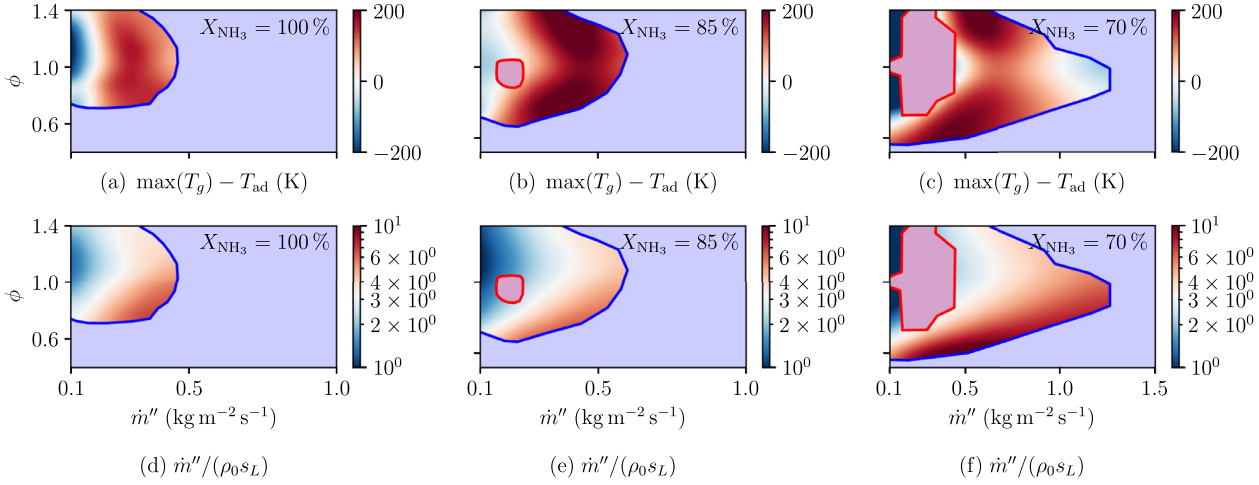

Fig. 13. (a–c): difference between the peak gas-phase temperature and adiabatic flame temperature $\max(T_g) - T_{ad}$. The red regions correspond to super-adiabatic combustion; (d–f): ratio of burner mass flux rate to the mass flux rate of a corresponding adiabatic freely propagating flame, $\dot{m}''/(\rho_0 s_L)$, where ρ_0 is the density of the unburnt gas and s_L is the adiabatic flame speed, as a function of equivalence ratio and mass flux rate for different X_{NH_3}. The blue curve marks the blowoff limit and the red shaded area indicates the flashback region. (For interpretation of the references to colour in this figure legend, the reader is referred to the web version of this article.)

ferred to as 1D–VAS–FP, in which the parameters for closure models used for 1D volume-averaged simulations are derived from first-principle simulations conducted on geometries directly extracted from µCT scans of the open-cell ceramic foams used in the burner. These properties include tortuosity, effective heat conductivity of the solid phase, and radiative extinction coefficient. The results show that the 1D–VAS–FP simulations compare well with measurements in terms of stability limits and exhaust gas composition when adequately determined effective properties are utilized. In contrast, when using empirical correlations found in the literature, volume-averaged simulations can no longer be considered as predictive. This demonstrates that volume-averaged models enable reliable predictions when utilizing constitutive models and effective properties derived from well-characterized geometries using first-principles methods—particularly when dealing with emerging fuels with challenging combustion properties. Regarding the capabilities of the 1D–VAS–FP modeling framework, the conclusions of this work are summarized as follows:

i. Using effective properties estimated from first-principle simulations together with the Schuster-Schwarzschild radiation model, predicted emissions of NO, unburnt NH_3 and H_2 are within 25% of the measurement uncertainties for most conditions, and experimental results are correctly reproduced;
ii. The 1D–VAS–FP modeling framework yields reliable stability limits for the burner. For operation with pure NH_3, 90% of all measured conditions are correctly captured by the 1D volume-averaged model. While blowoff limits are generally well predicted, flashback for high H_2 dilution is overpredicted. The high-velocity blow-off limit is also overpredicted, most likely due to flame wrinkling in this regime;
iii. At the same conditions, when utilizing closure models based on empirical correlations (1D–VAS–EMP), simulations are unreliable and largely overpredict blowoff and flashback limits. This is attributed to the much higher effective heat conductivity of the solid, leading to a much broader pre-heat region that extends into the flame arrestor integrated in the burner.

A limitation of this approach is that detailed geometric information of the porous matrix are required. These can typically be obtained using commonly available µCT, or, during the design phase of a PMB, using computer-assisted design tools. The availability of accurate bulk thermal properties for engineered ceramic materials used in PMB can also be an issue for predictive simulations [36].

Regarding the flame anchoring mechanism and pollutant formation in matrix-stabilized NH_3/H_2-air flames, the following conclusions were reached:

iv. At low mass flux rates, the peak gas-phase temperatures are below the adiabatic flame temperatures, leading to a broadening of the flame front inside the porous matrix. For most conditions within the stable operating range, peak temperatures exceed T_{ad} due to the internal heat recirculation, enabling super-adiabatic combustion.
iiv. Due to the effect of mass flux rates on peak temperatures, low mass flow rates result in lower NO and higher N_2O formation at lean conditions. At rich conditions, the lower solid temperatures at low mass flow rates result in higher unburnt NH_3 and lower H_2 emissions.
iiiv. Flame speeds can be increased tenfold in the PMB, which demonstrates that PMC can compensate for the low flame speed of NH_3 and yield high volumetric power densities.

The simulation code for 1D volume-averaged porous media combustion developed in this work is implemented in Cantera and publicly available [66].

Declaration of Competing Interest

The authors declare that they have no known competing financial interests or personal relationships that could have appeared to influence the work reported in this paper.

CRediT authorship contribution statement

Thorsten Zirwes: Conceptualization, Methodology, Investigation, Software, Validation, Writing – original draft. **Guillaume Vignat:** Conceptualization, Methodology, Investigation, Data curation, Writing – original draft. **Edna R. Toro:** Investigation, Data curation, Writing – review & editing. **Emeric Boigné:** Conceptualization, Methodology, Writing – review & editing. **Khaled Younes:** Investigation. **Dimosthenis Trimis:** Supervision, Funding acquisition. **Matthias Ihme:** Conceptualization, Methodology, Investigation, Supervision, Project administration, Funding acquisition, Writing – review & editing.

Acknowledgments

T. Zirwes and D. Trimis acknowledge the support of the PRIME program of the German Academic Exchange Service (DAAD) with funds from the German Federal Ministry of Education and Research (BMBF). E. Boigné was supported by the National Science Foundation with Award No. CBET-1800906. K. Younes gratefully acknowledges financial support from the U.S. Department of Energy, Office of Science under DOE (BES) Award DE-SC0022222. Part of this work was performed at the Stanford Nano Shared Facilities (SNSF), supported by the National Science Foundation under award ECCS-2026822. The authors thank Joseph C. Ferguson for helpful discussion on the utilization and extension of the PuMA analysis software.

References

[1] A. Valera-Medina, F. Amer-Hatem, A.K. Azad, I.C. Dedoussi, M. de Joannon, R.X. Fernandes, P. Glarborg, H. Hashemi, X. He, S. Mashruk, J. McGowan, C. Mounaim-Rouselle, A. Ortiz-Prado, A. Ortiz-Valera, I. Rossetti, B. Shu, M. Yehia, H. Xiao, M. Costa, Review on ammonia as a potential fuel: from synthesis to economics, Energy Fuels 35 (9) (2021) 6964–7029, doi:10.1021/acs.energyfuels.0c03685.

[2] H. Kobayashi, A. Hayakawa, K.D.K.A. Somarathne, E.C. Okafor, Science and technology of ammonia combustion, Proc. Combust. Inst. 37 (1) (2019) 109–133, doi:10.1016/j.proci.2018.09.029.

[3] L. Pizzuti, C.A. Martins, P.T. Lacava, Laminar burning velocity and flammability limits in biogas: a literature review, Renew. Sustain. Energy Rev. 62 (2016) 856–865.

[4] J.L. Ellzey, E.L. Belmont, C.H. Smith, Heat recirculating reactors: fundamental research and applications, Prog. Energy Combust. Sci. 72 (2019) 32–58.

[5] D. Trimis, F. Durst, Combustion in a porous medium: advances and applications, Combust. Sci. Technol. 121 (1–6) (1996) 153–168, doi:10.1080/00102209608935592.

[6] M.A. Mujeebu, M.Z. Abdullah, A.A. Mohamad, M.Z.A. Bakar, Trends in modeling of porous media combustion, Prog. Energy Combust. Sci. 36 (6) (2010) 627–650.

[7] H. Nozari, G. Karaca, O. Tuncer, A. Karabeyoglu, Porous medium based burner for efficient and clean combustion of ammonia–hydrogen–air systems, Int. J. Hydrogen Energy 42 (21) (2017) 14775–14785, doi:10.1016/j.ijhydene.2017.03.234.

[8] G. Vignat, B. Akoush, E.R. Toro Garza, E. Boigné, M. Ihme, Combustion of lean ammonia-hydrogen fuel blends in a porous media burner, Proc. Combust. Inst. 39 (2023) 4195–4204.

[9] D. Chen, J. Li, X. Li, L. Deng, Z. He, H. Huang, N. Kobayashi, Study on combustion characteristics of hydrogen addition on ammonia flame at a porous burner, Energy 263 (2023) 125613, doi:10.1016/j.energy.2022.125613.

[10] C. Keramiotis, M. Katoufa, G. Vourliotakis, A. Hatziapostolou, M.A. Founti, Experimental investigation of a radiant porous burner performance with simulated natural gas, biogas and synthesis gas fuel blends, Fuel 158 (2015) 835–842, doi:10.1016/j.fuel.2015.06.041.

[11] F. Song, Z. Wen, Z. Dong, E. Wang, X. Liu, Ultra-low calorific gas combustion in a gradually-varied porous burner with annular heat recirculation, Energy 119 (2017) 497–503, doi:10.1016/j.energy.2016.12.077.

[12] S.S. Su, S.J. Hwang, W.H. Lai, On a porous medium combustor for hydrogen flame stabilization and operation, Int. J. Hydrogen Energy 39 (36) (2014) 21307–21316.

[13] A.A.M. Oliveira, M. Kaviany, Nonequilibrium in the transport of heat and reactants in combustion in porous media, Prog. Energy Combust. Sci. 27 (5) (2001) 523–545.

[14] C. Wieland, C. Weis, P. Habisreuther, D. Trimis, 3D direct pore level simulations of radiant porous burners, Combust. Flame 245 (2022) 112370.

[15] P.-A. Masset, F. Duchaine, A. Pestre, L. Selle, Modelling challenges of volume-averaged combustion in inert porous media, Combust. Flame 251 (2023) 112678.

[16] I. Yakovlev, S. Zambalov, Three-dimensional pore-scale numerical simulation of methane-air combustion in inert porous media under the conditions of upstream and downstream combustion wave propagation through the media, Combust. Flame 209 (2019) 74–98.

[17] S. Sobhani, D. Mohaddes, E. Boigne, P. Muhunthan, M. Ihme, Modulation of heat transfer for extended flame stabilization in porous media burners via topology gradation, Proc. Combust. Inst. 37 (4) (2019) 5697–5704.

[18] D.A. Lawson, J. Norbury, Numerical solution of combustion in a porous medium, in: R.W. Lewis, K. Morgan (Eds.), Numerical Methods in Heat Transfer, Vol. 3, Wiley New York (1985), pp. 175–181.

[19] N. Djordjevic, P. Habisreuther, N. Zarzalis, A numerical investigation of the flame stability in porous burners employing various ceramic sponge-like structures, Chem. Eng. Sci. 66 (4) (2011) 682–688.

[20] G. Brenner, K. Pickenäcker, O. Pickenäcker, D. Trimis, K. Wawrzinek, T. Weber, Numerical and experimental investigation of matrix-stabilized methane/air combustion in porous inert media, Combust. Flame 123 (1–2) (2000) 201–213.

[21] R.S. Dhamrat, J.L. Ellzey, Numerical and experimental study of the conversion of methane to hydrogen in a porous media reactor, Combust. Flame 144 (4) (2006) 698–709.

[22] D.J. Diamantis, E. Mastorakos, D.A. Goussis, Simulations of premixed combustion in porous media, Combust. Theory Model. 6 (3) (2002) 383.

[23] S. Sobhani, B. Haley, D. Bartz, J. Dunnmon, J. Sullivan, M. Ihme, Investigation of lean combustion stability, pressure drop, and material durability in porous media burners, Turbo Expo: Power for Land, Sea, and Air, Vol. 5c, American Society of Mechanical Engineers (2017), pp. 1–12.

[24] M. Toledo, V. Bubnovich, A. Saveliev, L. Kennedy, Hydrogen production in ultra-rich combustion of hydrocarbon fuels in porous media, Int. J. Hydrogen Energy 34 (4) (2009) 1818–1827.

[25] A.J. Barra, G. Diepvens, J.L. Ellzey, M.R. Henneke, Numerical study of the effects of material properties on flame stabilization in a porous burner, Combust. Flame 134 (4) (2003) 369–379.

[26] M.J. Dixon, I. Schoegl, C.B. Hull, J.L. Ellzey, Experimental and numerical conversion of liquid heptane to syngas through combustion in porous media, Combust. Flame 154 (1–2) (2008) 217–231.

[27] M. Sahraoui, M. Kaviany, Direct simulation vs. volume-averaged treatment of adiabatic, premixed flame in a porous medium, Int. J. Heat Mass Transf. 37 (18) (1994) 2817–2834.

[28] J.-R. Shi, C.-M. Yu, B.-W. Li, Y.-F. Xia, Z.-J. Xue, Experimental and numerical studies on the flame instabilities in porous media, Fuel 106 (2013) 674–681.

[29] C. Bedoya, I. Dinkov, P. Habisreuther, N. Zarzalis, H. Bockhorn, P. Parthasarathy, Experimental study, 1D volume-averaged calculations and 3D direct pore level simulations of the flame stabilization in porous inert media at elevated pressure, Combust. Flame 162 (10) (2015) 3740–3754.

[30] R.C. Rocha, C.F. Ramos, M. Costa, X.S. Bai, Combustion of NH_3/CH_4/air and NH_3/H_2/air mixtures in a porous burner: Experiments and kinetic modeling, Energy Fuels 33 (12) (2019) 12767–12780, doi:10.1021/acs.energyfuels.9b02948.

[31] M. Bidi, M. Nobari, M.S. Avval, A numerical evaluation of combustion in porous media by EGM (Entropy Generation Minimization), Energy 35 (8) (2010) 3483–3500.

[32] P.A. Masset, O. Dounia, L. Selle, Fully explicit formulae for flame speed in infinite and finite porous media, Combust. Theory Model. 25 (5) (2021) 785–812, doi:10.1080/13647830.2021.1939422.

[33] M.R. Henneke, J.L. Ellzey, Modeling of filtration combustion in a packed bed, Combust. Flame 117 (4) (1999) 832–840.

[34] C.J. Tseng, Effects of hydrogen addition on methane combustion in a porous medium burner, Int. J. Hydrogen Energy 27 (6) (2002) 699–707.

[35] J.R. Howell, M.P. Mengüç, K. Daun, R. Siegel, Thermal radiation heat transfer, CRC Press, 2020.

[36] S. Sobhani, S. Allan, P. Muhunthan, E. Boigne, M. Ihme, Additive manufacturing of tailored macroporous ceramic structures for high-temperature applications, Adv. Eng. Mater. 22 (8) (2020) 1–8, doi:10.1002/adem.202000158.

[37] M. Kaviany, Principles of heat transfer in porous media, Springer Science & Business Media, 2012.

[38] S. Voss, M. Mendes, J. Pereira, S. Ray, J. Pereira, D. Trimis, Investigation on the thermal flame thickness for lean premixed combustion of low calorific H_2/CO mixtures within porous inert media, Proc. Combust. Inst. 34 (2) (2013) 3335–3342.

[39] M. Mendes, J. Pereira, J. Pereira, Calculation of premixed combustion within inert porous media with model parametric uncertainty quantification, Combust. Flame 158 (3) (2011) 466–476.

[40] X. Fu, R. Viskanta, J.P. Gore, Prediction of effective thermal conductivity of cellular ceramics, Int. Commun. Heat Mass Transfer 25 (2) (1998) 151–160.

[41] J.C. Ferguson, F. Panerai, A. Borner, N.N. Mansour, PuMA: the porous microstructure analysis software, SoftwareX 7 (2018) 81–87, doi:10.1016/j.softx.2018.03.001.

[42] N. Wakao, S. Kagei, Heat and mass transfer in packed beds, Vol. 1, Taylor & Francis, 1982.

[43] L.B. Younis, R. Viskanta, Experimental determination of the volumetric heat transfer coefficient between stream of air and ceramic foam, Int. J. Heat Mass Transf. 36 (6) (1993) 1425–1434.

[44] H. Liu, S. Dong, B.-W. Li, H.-G. Chen, Parametric investigations of premixed methane–air combustion in two-section porous media by numerical simulation, Fuel 89 (7) (2010) 1736–1742.

[45] M. Scheffler, P. Colombo, Cellular ceramics: structure, manufacturing, properties and applications, John Wiley & Sons, 2006.

[46] H.T. Hamad, D.W. Abbood, A.S. Mustafa, Strength tortuosity-porosity relation in locally types of porous media (experimental model), IOP Conference Series: Materials Science and Engineering, Vol. 454, IOP Publishing (2018), p. 012093.

[47] S.-Y. Hsu, The effects of tortuosity and dispersion on porous combustion, Combust. Theory Model. 25 (7) (2017) 1175–1194.

[48] F. Kuwahara, M. Shirota, A. Nakayama, A numerical study of interfacial convec-

tive heat transfer coefficient in two-energy equation model of porous media, Int. J. Heat Mass Transf. 44 (1) (2000) 1153–1159.
[49] R. Habib, N. Karimi, B. Yadollahi, M.H. Doranehgard, L.K.B. Li, A pore-scale assessment of the dynamic response of forced convection in porous media to inlet flow modulations, Int. J. Heat Mass Transf. 153 (2020) 119657, doi:10.1016/j.ijheatmasstransfer.2020.119657.
[50] P. Habisreuther, N. Djordjevic, N. Zarzalis, Statistical distribution of residence time and tortuosity of flow through open-cell foams, Chem. Eng. Sci. 64 (23) (2009) 4943–4954.
[51] A.J. Barra, J.L. Ellzey, Heat recirculation and heat transfer in porous burners, Combust. Flame 137 (1–2) (2004) 230–241.
[52] J.C. Ferguson, A. Borner, F. Panerai, S. Close, N.N. Mansour, Continuum to rarefied diffusive tortuosity factors in porous media from x-ray microtomography, Comput. Mater. Sci 203 (2022) 111030.
[53] K.M. Graczyk, M. Matyka, Predicting porosity, permeability, and tortuosity of porous media from images by deep learning, Sci. Rep. 10 (1) (2020) 21488.
[54] M. Ihme, W.T. Chung, A.A. Mishra, Combustion machine learning: principles, progress and prospects, Prog. Energy Combust. Sci. 91 (2022) 101010.
[55] G. Zhang, Q. Li, X. Liu, B. Lin, X. Li, Numerical investigation on lean methane combustion with modified effective thermal conductivity of the porous media, Combust. Theory Model. 26 (2) (2021) 365–382.
[56] G. Vignat, T. Zirwes, E.R. Toro Garza, K. Younes, E. Boigné, P. Muhunthan, L. Simitz, D. Trimis, M. Ihme, Experimental and numerical investigation of flame stabilization and pollutant formation in matrix stabilized ammonia-hydrogen combustion, Combust. Flame 250 (2023) 112642.
[57] C.E. Baukal, P.B. Eleazer, Quantifying NO_x for industrial combustion processes, J. Air Waste Manage. Assoc. 48 (1) (1998) 52–58, doi:10.1080/10473289.1998.10463664.
[58] J.R. Howell, M.J. Hall, J.L. Ellzey, Combustion of hydrocarbon fuels within porous inert media, Prog. Energy Combust. Sci. 22 (2) (1996) 121–145.
[59] R.J. Kee, M.E. Coltrin, P. Glarborg, Chemically reacting flow: theory and practice, John Wiley & Sons, 2005.
[60] P.-f. Hsu, J.R. Howell, Measurements of thermal conductivity and optical properties of porous partially stabilized zirconia, Exp. Heat Transf. Int. J. 5 (4) (1992) 293–313.
[61] M. Pelanconi, M. Barbato, S. Zavattoni, G.L. Vignoles, A. Ortona, Thermal design, optimization and additive manufacturing of ceramic regular structures to maximize the radiative heat transfer, Mater. Des. 163 (2019) 107539.
[62] A. Stagni, C. Cavallotti, S. Arunthanayothin, Y. Song, O. Herbinet, F. Battin-Leclerc, T. Faravelli, An experimental, theoretical and kinetic-modeling study of the gas-phase oxidation of ammonia, React. Chem. Eng. 5 (4) (2020) 696–711, doi:10.1039/c9re00429g.
[63] X. Zhang, S.P. Moosakutty, R.P. Rajan, M. Younes, S.M. Sarathy, Combustion chemistry of ammonia/hydrogen mixtures: jet-stirred reactor measurements and comprehensive kinetic modeling, Combust. Flame 234 (2021) 111653.
[64] Y. Jiang, A. Gruber, K. Seshadri, F. Williams, An updated short chemical-kinetic nitrogen mechanism for carbon-free combustion applications, Int. J. Energy Res. 44 (2020) 795–810.
[65] D.G. Goodwin, R.L. Speth, H.K. Moffat, B.W. Weber, Cantera: An object-oriented software toolkit for chemical kinetics, thermodynamics, and transport processes, 2021. https://www.cantera.org.
[66] PMCToolbox: a Cantera extension for simulating 1D flames in porous media. https://github.com/IhmeGroup/PMCToolbox.
[67] M. Kuwahara, K. Hachimura, S. Eiho, M. Kinoshita, Processing of RI-angiocardiographic images, Digital Processing of Biomedical Images, Springer (1976), pp. 187–202.
[68] N. Otsu, A threshold selection from gray-level histograms, IEEE Trans. Syst. Man Cybern. SMC-9 (1) (1979) 62–66, doi:10.1109/tsmc.1979.4310076.
[69] J.C. Ferguson, F. Semeraro, J.M. Thornton, F. Panerai, A. Borner, N.N. Mansour, Update 3.0 to PuMA: the porous microstructure analysis software, (PII:S2352711018300281), SoftwareX 15 (2021) 100775, doi:10.1016/j.softx.2021.100775.
[70] O. Nilsson, H. Mehling, R. Horn, J. Fricke, R. Hofmann, S.G. Müller, R. Eckstein, D. Hofmann, Determination of the thermal diffusivity and conductivity of monocrystalline silicon carbide (300–2300 K), High Temp. - High Pressures 29 (1) (1997) 73–79, doi:10.1068/htec142.
[71] G.A. Slack, Thermal conductivity of pure and impure silicon, silicon carbide, and diamond, J. Appl. Phys. 35 (12) (1964) 3460–3466, doi:10.1016/S0375-9601(98)00347-8.
[72] D.M. Liu, B.W. Lin, Thermal conductivity in hot-pressed silicon carbide, Ceram. Int. 22 (5) (1996) 407–414, doi:10.1016/0272-8842(95)00125-5.
[73] K. Terrani, B. Jolly, M. Trammell, 3D printing of high-purity silicon carbide, J. Am. Ceram. Soc. 103 (3) (2020) 1575–1581, doi:10.1111/jace.16888.
[74] K. Pelissier, T. Chartier, J.M. Laurent, Silicon carbide heating elements, Ceram. Int. 24 (5) (1998) 371–377, doi:10.1016/S0272-8842(97)00024-2.
[75] N.P. Bansal, D. Zhu, Thermal conductivity of zirconia-alumina composites, Ceram. Int. 31 (7) (2005) 911–916, doi:10.1016/j.ceramint.2004.09.018.
[76] G. Pia, L. Casnedi, U. Sanna, Porosity and pore size distribution influence on thermal conductivity of yttria-stabilized zirconia: experimental findings and model predictions, Ceram. Int. 42 (5) (2016) 5802–5809, doi:10.1016/j.ceramint.2015.12.122.
[77] K.W. Schlichting, N.P. Padture, P.G. Klemens, Thermal conductivity of dense and porous yttria-stabilized zirconia, J. Mater. Sci. 36 (12) (2001) 3003–3010, doi:10.1023/A:1017970924312.
[78] E. Maire, P. Colombo, J. Adrien, L. Babout, L. Biasetto, Characterization of the morphology of cellular ceramics by 3D image processing of X-ray tomography, J. Eur. Ceram. Soc. 27 (4) (2007) 1973–1981, doi:10.1016/j.jeurceramsoc.2006.05.097.
[79] J. Gostick, Z. Khan, T. Tranter, M. Kok, M. Agnaou, M. Sadeghi, R. Jervis, et al., PoreSpy: a Python toolkit for quantitative analysis of porous media images, J. Open Source Softw. 4 (37) (2019) 1296, doi:10.21105/joss.01296.
[80] R.J. Kee, F.M. Rupley, E. Meeks, J.A. Miller, CHEMKIN-III: A FORTRAN chemical kinetics package for the analysis of gas-phase chemical and plasma kinetics, Technical Report, Sandia National Laboratories (SNL-CA), Livermore, CA (United States), 1996.
[81] G. Guennebaud, B. Jacob, et al., Eigen v3, 2010, (http://eigen.tuxfamily.org).
[82] J.C. Ferguson, S. Sobhani, M. Ihme, Pore-resolved simulations of porous media combustion with conjugate heat transfer, Proc. Combust. Inst. 38 (2) (2021) 2127–2134, doi:10.1016/j.proci.2020.06.064.
[83] R.V. Fursenko, I.A. Yakovlev, E.S. Odintsov, S.D. Zambalov, S.S. Minaev, Pore-scale flame dynamics in a one-layer porous burner, Combust. Flame 235 (2022) 111711.
[84] A.H. Murphy, The Finley affair: a signal event in the history of forecast verification, Weather Forecasting 11 (1) (1996) 3–20.
[85] S. Mashruk, E.C. Okafor, M. Kovaleva, A. Alnasif, D.G. Pugh, A. Hayakawa, A. Valera-Medina, Evolution of N_2O production at lean combustion condition in NH_3/H_2/air premixed swirling flames, Combust. Flame 244 (2022) 112299, doi:10.1016/j.combustflame.2022.112299.